Supporting Information

Light-Induced Capacitance Tunability in Ferroelectric Crystals

David Páez-Margarit,[‡] *Fernando Rubio-Marcos,*[*,§] *Diego A. Ochoa,*[‡] *Adolfo Del Campo,*[§] *José F. Fernández,*[§] *and José E. García**[*,‡]

[‡]Department of Physics, Universitat Politècnica de Catalunya, 08034 Barcelona, Spain.

[§]Department of Electroceramics, Instituto de Cerámica y Vidrio – CSIC, 28049 Madrid, Spain

Corresponding Authors

*E-mail: jose.eduardo.garcia@upc.edu (J.E.G.).

*E-mail: frmarcos@icv.csic.es (F.R-M.).

1. Materials and Methods

Samples: $BaTiO_3$ (BTO) single crystals were produced by top-seeded solution growth and provided by PIKEM Ltd (UK). The 5 × 5 × 0.5 mm BTO crystals were grown with two different crystalline orientations. One sample was grown with (100) orientation or *a*-plane, while the other sample was grown with (001) orientation or *c*-plane. A detailed characterization of the domain structure of both samples can be found in Figure S3 and S4. The large crystal faces were sputtered with an indium tin oxide (ITO) layer. ITO was chosen as a transparent contact in order to let the laser light fall on the BTO crystal.

Confocal Raman Microscopy (CRM): A Witec alpha-300RA confocal Raman microscope was used to determinate the ferroelectric domain structures of both (100) and (001) BTO single crystals. Raman maps of the surface and the cross-section with an area of 150 × 20 μm were performed with a 100X objective lens and numerical aperture of 0.95. Raman images were created by 150 x 20 pixels (3000 pixels), an acquisition time for a pixel of 0.2 s and an incident laser power of 40 mW, requiring 10 min for each Raman map. Finally, the collected data were analyzed by using Witec Control Plus Software.

Atomic Force Microscopy (AFM): An AFM coupled to the Witec alpha-300RA confocal Raman microscope was used to obtain the topographic information of the samples. AFM images were taken in non-contact mode and using gold-coated silicon (with a resonant frequency of 268 kHz). Under these conditions, AFM images were captured by scanning 136 lines with 1024 points per line. The selected areas (150 × 20 μm) were those previously studied by CRM.

2. Details of the Experimental Setup for Capacitance Measurements

The setup was designed in order to assemble a versatile experimental system to carry out the desired novel experiments. The main part of the setup is shown in Figure S1, which may adopt different configurations depending on the laser used (a green 532 nm, a red 658 nm or a blue-violet 405 nm wavelength laser) and on the experiment to be performed. Thus, the ND filter is used only for power dependence experiments, and the powermeter is placed in the line of light only for checking the light power. The laser diode mount is fed by a dc power supply that is programmed according to the laser diode characteristics. All measurements are automatically taken by using an impedance analyzer controlled by a computer.

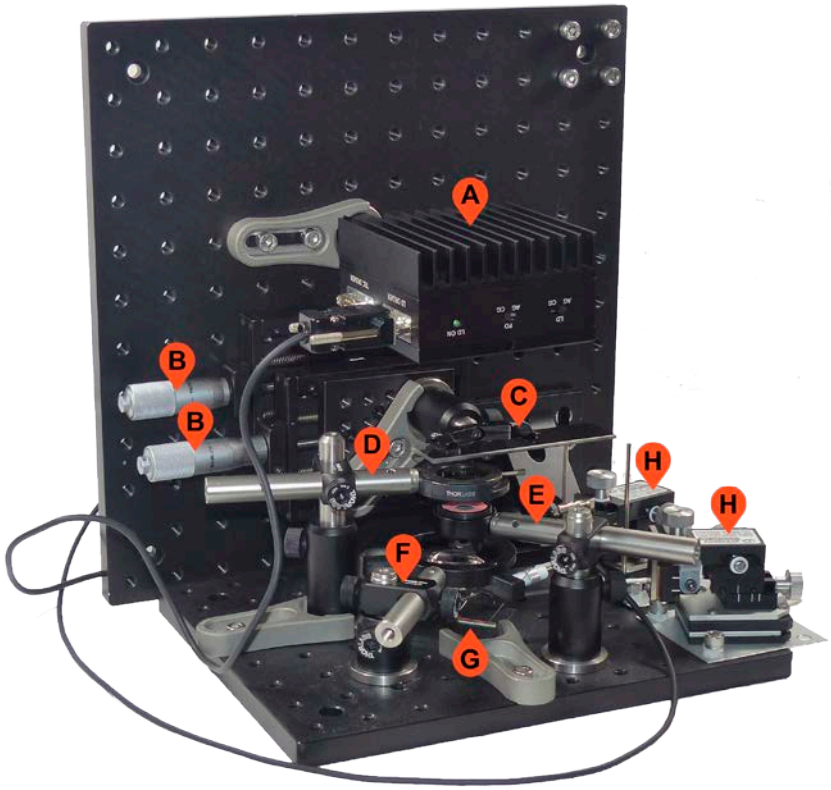

Figure S1 | Main experimental setup for capacitance measurements. The setup consists of a laser diode mount (A), support micropositioners (B) for the ND filter (C), iris (D), powermeter (E), plano-convex lens (F), sample holder (G) and contact micropositioners (H). The sample is located in a 3D printed custom-made sample holder perpendicular to the line of light.

The incident light effect on the thermal behavior of the ITO/BTO/ITO capacitors was studied prior to the dielectric measurements. To that end**,** the sample was placed in an experimental system equipped with a thermal camera (FLIR Systems T440) for testing the sample temperature under illumination. A simple off-on-off light switching experiment was carried out using a green (532 nm) laser as the light source. The FLIR Tools+ software was used for image recording and data acquisition, and the results are shown in Figure S2. As may be observed, the sample temperature increases by only 3.2 ºC, despite the extreme condition of the experiment; that is, under a light power of 60 mW and an exposure time of ~10 min. This increase in temperature produces no noticeable changes in the dielectric constant of BTO crystals.[1] The experiment provides an irrefutable proof that thermal effects are not at the core of the light-induced dielectric constant tunability reported in this work.

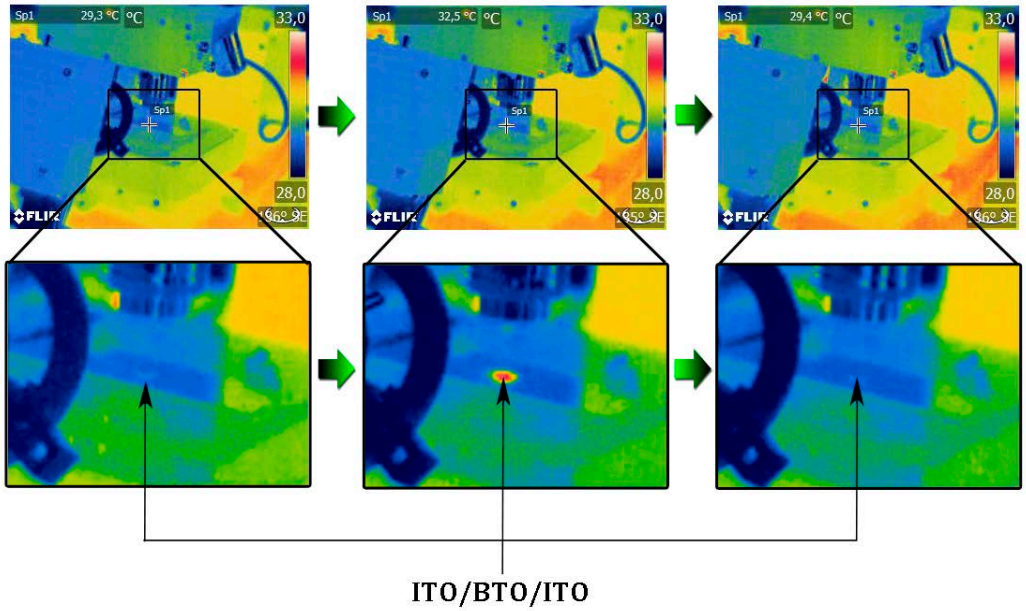

Figure S2 | Thermal behavior of the ITO/BTO/ITO capacitors. Starting from an off state (29.3 ºC, left panel), the sample is irradiated with laser light until the temperature of the sample stabilizes at a maximum value (32.5 ºC, central panel). The illumination is then turned off again, and after some minutes the sample reaches thermal equilibrium with the environment (29.4 ºC, right panel). A diode laser of 532 nm of wavelength and 60 mW of power is used as the light source.

In order to experimentally evaluate how an increase of ~3 ºC disturb the dielectric response of the BTO crystal, a reference measurement of the dielectric constant of the crystal under conventional heating was performed. Figure S3 shows the result. As expected for a (100)-oriented BTO crystal, the dielectric constant decrease as the temperature rises in temperatures around room temperature.[2] As may be observed, an increase of 3ºC supposes a decrease of the dielectric constant less than 3%. More than 10 degrees (~14 K) of temperature increase are required to reach a decrease in the dielectric constant comparable to that produced by the illumination at 40 mW (Figure 1a of the main manuscript). In conclusion, this fact is an undeniable experimental proof that a local optical heating is not at the core of the light-induced dielectric constant tunability reported in this work.

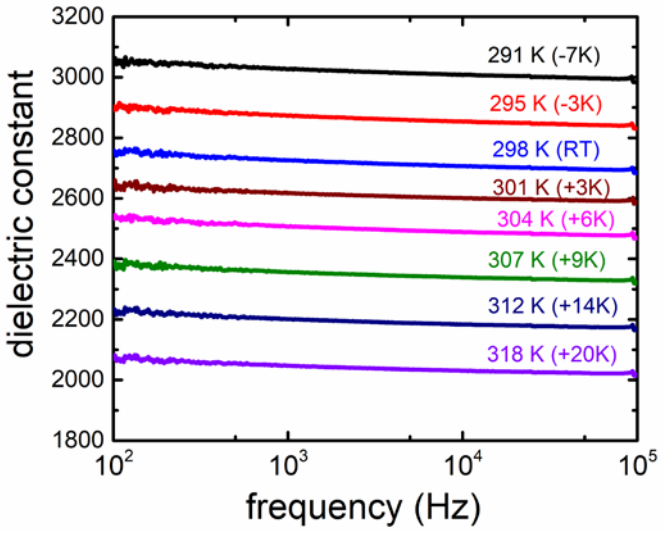

Figure S3 | Dielectric constant as a function of the frequency at several temperatures around room temperature (RT). The measurements were performed using an impedance analyser HP4294A in the frequency range 100 Hz to 100 kHz The sample was placed in a controlled temperature chamber. The sample temperature was monitorized and each measure was carried out once the temperature was stabilized.

3. Domain Structure Characterization of the (100) $BaTiO_3$ Single Crystal

A complete identification of the structure and the crystalline orientation of the BaTiO3 (BTO) crystal were carried out by confocal Raman microscopy (CRM) combined with atomic force microscopy (AFM) in the same experimental setup, thereby giving direct correlations between topography and local structure. Figure S4a shows the optical image of the (100) BTO crystal surface. The Raman images, both at the surface (Figure S4b) and the cross section (Figure S4c), display a domain structure composed of *a*-domains (red domains), *c*-domains (blue domains) and *b*-domains (green domains). These latter appear in the *a*-*c*-domain wall within the ($\{101\}_{pc}$) plane, as may be observed in Figure S4c. Additionally, the main Raman spectra of Raman images associated with different types of domains on the BTO crystal are represented in Figure S4d. Note that the *a*-domains are easily traceable, since they are characterized by the annihilation of two Raman modes[3] (specifically, by the annihilation of Raman modes marked 4 and 6 in Figure S4d), which can be assigned through the Table S1. Consequently, red and blue spectra correspond to *a*- and *c*-domains, respectively. Furthermore, we detected more than one *b*-domain (shown in green) that hindered only the *a*-*c*-domain wall (Figure S4c). A set of parallel *b*-domains exist that grow in the *c*-domains region. The Raman spectrum of the *b*-domain is clearly a combination of *a*-domain and *c*-domain Raman spectra (Figure S4d).

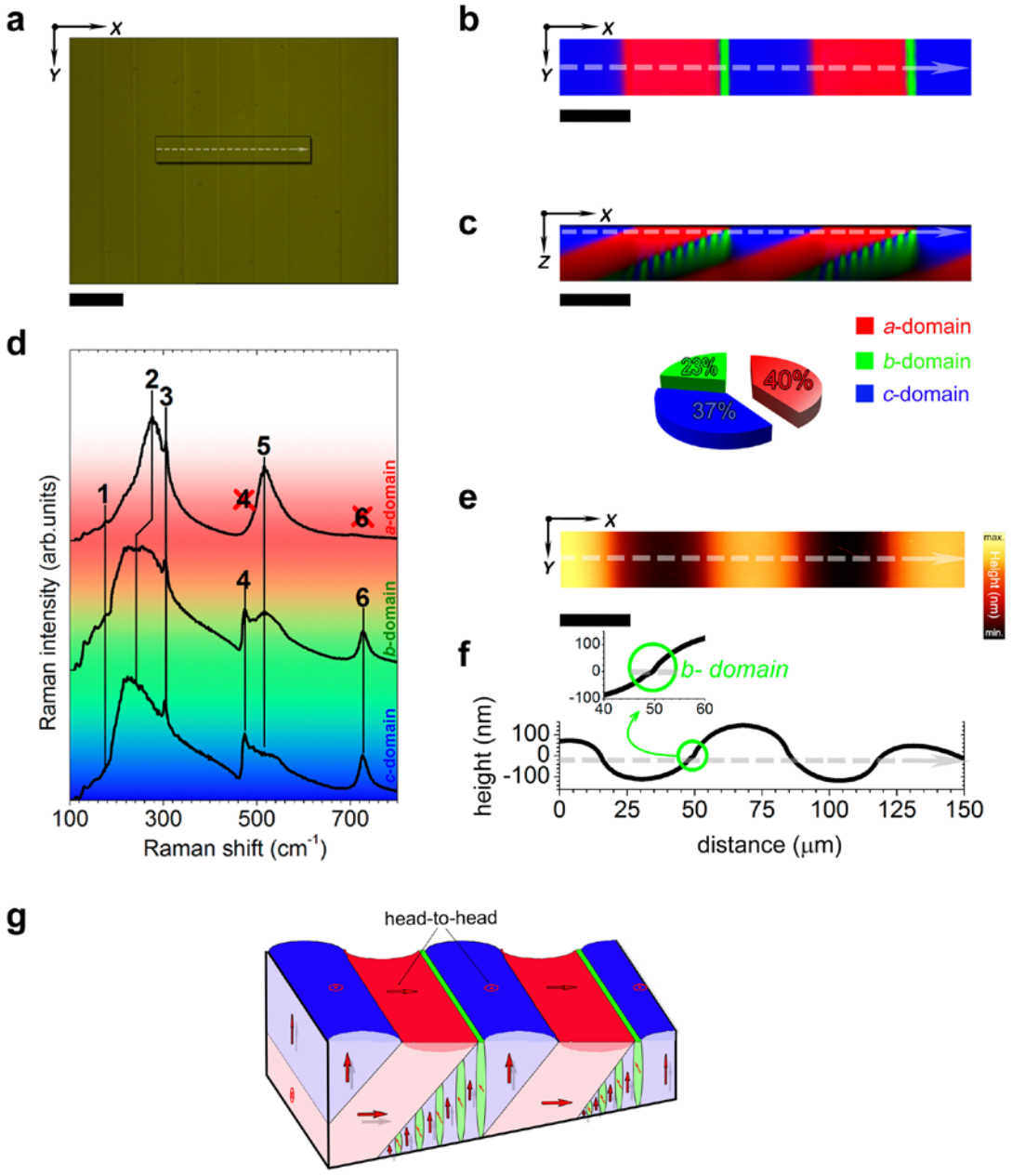

Figure S4 | Domain structure of a BTO single crystal grown with (100) orientation. (**a**) Optical micrograph of the (100) BTO single crystal. The white rectangle shows the scanned area. Scale bar, 50 μm. Raman image showing the domain distribution at the surface (**b**) and the cross section (**c**) of the crystal by Confocal Raman Microscopy (CRM). Scale bar, 25 μm. In relation to their nature, the domains can be categorized into different types labelled as *a*-domains, *b*-domains and *c*-domain, which are represented in red, green and blue, respectively. Additionally, relative area fractions of each domain are indicated at the bottom of the Raman images, which were calculated from **c**. (**d**) The main Raman spectra of BTO Raman image associated with different types of domains. The numbers next to the vibrational peaks represent the main atomic motions (the assignment of the Raman modes are shown in Table S1). The panel (**e**) displays the AFM image of crystal, showing the domain topography inside the marked white box of **a**. Scale bar, 25 μm. (**f**) AFM topography scan along the white dashed line of **a**-**c**. The insert in panel **f** shows a detail of the domain boundary topography, corresponding to the presence of a *b*-domain located close to the *a*-*c* domain wall. (**g**) Schematic view of the domain structure of the sample, built from a combination of AFM and Raman mapping information.

Additionally, we focus our attention on morphology across different domains for the analyses of the topographical features at local scale, in the same region previously studied by CRM. These features are indicated in Figure S4e, while the AFM scan reveals the domain boundary topography, which is associated with soft transitions (Figure S4f). These results, together with the Raman information, suggest that the *c*-domain protrudes accordingly with out-of-plane distortion, while the *a*-domain is depleted. By contrast, these transitions are asymmetric as a consequence of the intersection with the *b*-domains close to *a*-*c*-domain walls (see insert in Figure S4f). Note that the *b*-domains are generated by high-stress degree accumulation, and are directly associated with the formation of "charged domain walls" (CDWs), as established in other works.[4-6]

Table S1 | Raman modes and their mode symmetry assignments in the tetragonal $BaTiO_3$ single crystal. The table summarizes both symmetry and nature (first and second order) of the Raman modes of the $BaTiO_3$ phase. According to the nuclear site group analysis, Raman active phonons of the tetragonal P4mm (C_{4v}^1) crystal symmetry are represented by $3A_1 + B_1 + 4E$. Long-range electrostatic forces induce the splitting of transverse and longitudinal phonons, which results in split Raman active phonons represented by $3[A_1\,(TO) + A_1\,(LO)] + B_1 + 4[E\,(TO) + E\,(LO)]$.

Raman Shift (cm^{-1})	**Symmetry**	**Abbreviated** number	**Reference**
36	E (TO)	**1**	7-11
170	A_1 (TO)		8-13
180	E (TO_2), E (LO)		7-11
185	A_1 (LO)		8-13
210-270	A_1 (TO_2)	**2**	8-13
305	E ($TO_3 + LO_2$)	**3**	7-11
305	B_1		7-11
463	E (LO_3)	**4**	7-11
475	A_1 (LO_2)		8-13
486	E (TO_4)		7-11
518	E (TO_5)	**5**	7-11
520	A_1 (TO_3)		8-13
715	E (LO_4)	**6**	7-11
720	A_1 (LO_3)		8-13

Finally, the above results constitute the basis for building a schematic view of the domain structure of the BTO single crystal grown with (100) orientation (Figure S4g). The (100) BTO crystal contains *a*-domains, with polarization parallel to the crystal surface; *c*-domains, with polarization perpendicular to the crystal surface, and *b*-domains with polarization at ~45º to the crystal surface. This configuration leads to the formation of two different types of 90º domain walls; *a*-*c*- and *c*-*a*-domain walls. In accordance with our previous observations,[4,5] the *a*/*c*-domain wall is a transition zone of mixed polarization, which is composed of *c*-domains and *a*-domains with a head-to-head (H-H) configuration of the polarization vectors. The H-H configuration maximizes the internal stress close to the domain wall,[4,5] and consequently the *a*-*c*-domain walls are hindered by *b*-domains. By contrast, the *c*-*a*-domain wall has a tail-to-tail (T-T) configuration of the polarization vectors, resulting in weakly charged domain walls (wCDW). More importantly, there is no presence of *b*-domains as a result of a low stress degree.

4. Domain Structure Characterization of the (001) $BaTiO_3$ Single Crystal

To evaluate the impact of the crystalline orientation on the light-activated phenomenon, and therefore to determine its relationship with the domain structure, we have revealed the domain structure for a (001) BTO crystal. Figure S5a shows the optical micrograph of the (001) BTO single crystal, in which the area scanned by CRM and AFM (depicted by the white rectangle) has been marked. As observed by CRM (Figure S5b and S5c), the same three domain types can be identified as follows: *a*-domains (depicted in red), *c*-domains (depicted in blue) and *b*-domains (depicted in green). Regarding the topography, its main features are indicated in Figure S4d, while the AFM scan reveals the domain boundary topography associated with an asymmetric saw-teeth transition, as depicted in Figure S5e.

Although both BTO crystals have similarities (that is, they have the same three domain types), their differences are greater. We can make some clear morphology differences from the CRM and AFM observations: (*i*) the (100) BTO crystal shows a balance in the domain width for the *a*-domains and *c*-domains, which are basically constituted by a mean domain width of ~32 μm (see Figure S4b-c and S4e-f). By contrast, the (001) BTO crystal develops an asymmetric domain width and the *c*-domains have a width of ~19 μm, while the *a*-domains are clearly smaller with a mean domain width of ~6 μm (Figure S5b-e). This fact leads us to the following observation directly related with the *b*-domains: (*ii*) the stack of *b*-domains (that is, *b*-domain density) caused by the domain wall between *a*- and *c*-domains in the (100) BTO crystal is larger than the *b*-domain density in the (001) BTO crystal, as a result of the greater accumulation of the local stress in the (100) BTO crystal. Considering that the *b*-domain is the most sensitive to the light, we intuit that its domain density should play a key role in the light-induced phenomenon here studied.

To sum up, we have built a representative scheme of the domain structure for the BTO single crystal grown with (001) orientation (Figure S5f), in which we have captured the most relevant features of the observations derived from CRM and AFM results.

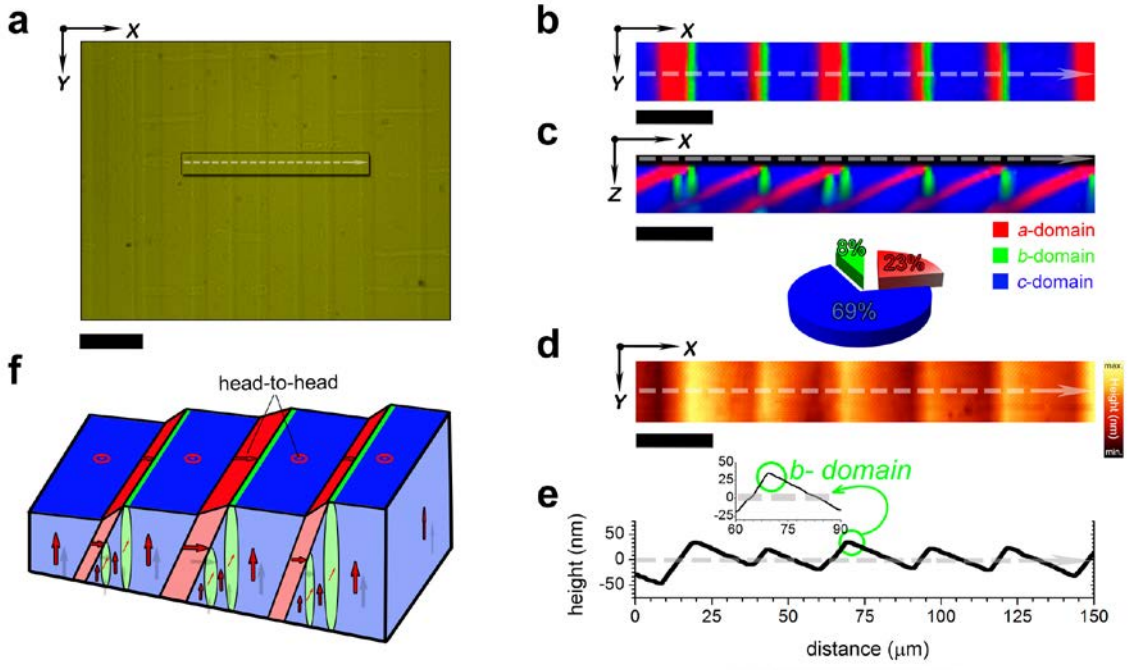

Figure S5 | Domain structure of a BTO single crystal grown with (001) orientation. (**a**) Optical micrograph of the (001) BTO single crystal. The white rectangle shows the scanned area. Scale bar, 50 μm. Raman image showing the domain distribution at the surface (**b**) and the cross section (**c**) of the crystal by Confocal Raman Microscopy (CRM). Scale bar, 25 μm. In relation to their nature, the domains can be categorized into different types labelled as *a*-domain, *b*-domains and *c*-domain, which are represented in red, green and blue, respectively. Additionally, relative area fractions of each domain are indicated at the bottom of panel **c**. Panel (**d**) displays the AFM image of the surface crystal, in which the domain topography inside the marked white box of **a** is shown. Scale bar, 25 μm. (**e**) AFM topography scan along the white dashed line of **a**-**c**. The insert in panel **e** shows a detail of the domain boundary topography, corresponding to the presence of a *b*-domain located close to the *a*-*c* domain wall. (**f**) Schematic domain wall structures derived from AFM and Raman mapping information.

Supplementary References

(1) Kay, H. F.; Vousden, P. Symmetry Changes in Barium Titanate at Low Temperatures and Their Relation to Its Ferroelectric Properties. *Philos. Mag*. **1949**, *40*, 1019-1040.

(2) von Hippel, A. Ferroelectricity, Domain Structure, and Phase Transitions of Barium Titanate. *Rev. Mod. Phys.* **1950**, *22*, 221-237.

(3) Pezzotti, G.; Okai, K.; Zhu, W. Stress Tensor Dependence of the Polarized Raman Spectrum of Tetragonal Barium Titanate. *J. Appl. Phys.* **2012**, *111*, 013504.

(4) Rubio-Marcos, F.; Del Campo, A.; Marchet, P.; Fernández, J. F. Ferroelectric Domain Wall Motion Induced by Polarized Light. *Nat. Comm.* **2015**, *6*, 6594.

(5) Rubio-Marcos, F.; Ochoa, D. A.; Del Campo, A.; García, M. A.; Castro, G. R.; Fernández, J. F.; García, J. E. Reversible Optical Control of Macroscopic Polarization in Ferroelectrics. *Nat. Photon*. **2018**, *12*, 29-32.

(6) Deng, H.; Zhang, H.; Zhao, X.; Chen, C.; Wang, X.; Li, X.; Lin, D.; Ren, B.; Jiao, J.; Luo, H. Direct Observation of Monoclinic Ferroelectric Phase and Domain Switching Process in $(K_{0.25}Na_{0.75})NbO_3$ Single Crystals. *CrystEngComm* **2015**, *17*, 2872-2877.

(7) DiDomenico, M.; Wemple, S. H.; Porto, S. P. S.; Bauman, R. P. Raman Spectrum of Single-Domain $BaTiO_3$. *Phys. Rev.* **1968,** *174*, 522-530**.**

(8) Venkateswaran, U. D.; Naik, V. M.; Naik, R. High-pressure Raman Studies of Polycrystalline $BaTiO_3$. *Phys. Rev. B* **1998**, *58*, 14256-14260.

(9) Dobal, P. S.; Katiyar, R. S. Studies on Ferroelectric Perovskites and Bi-layered Compounds Using Micro-Raman Spectroscopy. *J. Raman Spectrosc.* **2002**, *33*, 405-423.

(10) Shiratori, Y.; Pithan, C.; Dornseiffer, J.; Waser, R. Raman Scattering Studies on Nanocrystalline $BaTiO_3$ Part I—Isolated Particles and Aggregates. *J. Raman Spectrosc.* **2007**, *38*, 1288-1299.

(11) Shiratori, Y.; Pithan, C.; Dornseiffer, J.; Waser, R. Raman Scattering Studies on Nanocrystalline $BaTiO_3$ Part II—Consolidated Polycrystalline Ceramics. *J. Raman Spectrosc.* **2007**, *38*, 1300-1306.

(12) Pinczuk, A.; Taylor, W. T.; Burstein, E.; Lefkowitz, I. The Raman Spectrum of $BaTiO_3$. *Solid State Commun.* **1967**, *5*, 429-433.

(13) Burns, G.; Scott, B. Raman Scattering in the Ferroelectric System $Pb_{1-x}Ba_xTiO_3$. *Solid State Commun.* **1971**, *9*, 813-817.